# Global Multivariate Spectral Analysis of Mercury and the Identification of Geochemical Terrains: Derived from the MASCS Spectrometer onboard NASA's MESSENGER Mission

**I. Varatharajan[1], M. D'Amore[1], D. L. Domingue[2], J. Helbert[1], and A. Maturilli[1]**

[1]Institute for Planetary Research, German Aerospace Center DLR, Rutherfordstraße 2, 12489 Berlin, Germany.

[2]Planetary Science Institute, Tucson AZ, 85719, USA.

Corresponding author: Indhu Varatharajan (indhu.varatharajan@dlr.de)

**Key Points:**

- K-Means clustering of global MASCS hyperspectral datacube suggests that most of Mercury's surface fall into two contiguous regions.
- Principal component analysis (PCA) of MASCS datacube distinguishes the northern volcanic plains as consisting of high-Mg and low-Mg terrains.
- The 6$^{th}$ component of a Principal Component Analysis of MASCS data correlates with physical properties of Mercury surface associated with fine-grained, freshly exposed materials.

## Abstract

The visible-infrared spectra of Mercury's surface show little variation, displaying no distinct spectral features except for the possible spectral identification of sulfide within the hollows (Vilas et al. 2016). It is essential therefore to define and map any subtle spectral heterogeneity across Mercury's surface and to correlate these differences where possible to geomorphological features, such as impact craters, volcanic vents, and tectonic features. The Mercury Atmospheric and Surface and Composition Spectrometer (MASCS) instrument onboard MESSENGER spacecraft is the only hyperspectral reflectance spectrometer to date that has mapped Mercury's surface in the wavelength range 320 nm - 1450 nm. The limitation of MASCS is that it's a point spectrometer that mapped Mercury's surface at non-uniform spatial scale. In this study, we resampled the global MASCS hyperspectral dataset to a uniform spatial resolution of 1 pixel per degree. This enabled us to perform global multivariate analyses, including standard spectral parameter maps, k-means clustering, and principal component analysis (PCA) to spectrally characterize Mercury's surface. Among these techniques, PCA significantly improved the identification of spectral heterogeneities across Mercury correlated to both chemical and physical properties of the surface, enabling us to identify units based on grain size, the presence of amorphous materials, and space-weathering associated alterations. The global MASCS PC color composite map derived from principal components 1, 2, and 6 effectively distinguishes varying spectro-morphologies across Mercury's surface, thus highlighting the spectral properties of various geochemical terrains. We further demonstrate that PCA spectrally differentiates between the two northern volcanic plains' geochemical regions; the high-Mg and low-Mg terrains.



## Plain Language Summary

Different minerals absorb the energy from sunlight at different wavelengths of the electromagnetic spectrum. Therefore, spectra measured over a wide range of wavelengths can be used as finger-prints to identify minerals using remote-sensing observations. In this study, we used the hyperspectral visible-infrared spectrometer, Mercury Atmospheric and Surface and Composition Spectrometer (MASCS) onboard NASA's MESSENGER spacecraft, to map the spectral heterogeneity across Mercury's surface. MASCS mapped Mercury's surface at varying spatial resolution (i.e., each pixel maps the surface at varying areal dimensions). In this study we created a global MASCS spectral dataset with a uniform resolution of ~42.5 km/pixel. This enabled us to perform comparable global statistical analyses across Mercury's surface to characterize its spectral properties. The study found that principal component analysis (PCA) significantly improves the identification of spectral heterogeneities across Mercury correlated with both chemical and physical properties of the surface. This technique enabled us to identify spatial units based on grain size, the presence of amorphous materials, and space-weathering associated alterations. One of the highlights is that PCA spectrally differentiates between the two northern volcanic plains regions, one consisting of high-Mg and the other low-Mg terrains.


## 1 Introduction

The MErcury Surface, Space ENvironment, GEochemistry, and Ranging (MESSENGER) mission was the first spacecraft to orbit Mercury. Over its 4 years at Mercury, beginning with its orbit insertion in 2011 (Solomon et al., 2001), the instruments onboard this

spacecraft globally mapped the planet. Among the seven scientific instrument suites, MESSENGER carried three spectrometers and one camera system. These included an X-Ray Spectrometer (XRS), a Gamma-Ray and Neutron Spectrometer (GRNS), the Mercury Atmospheric and Surface Composition Spectrometer (MASCS), and the Mercury Dual Imaging System (MDIS), all of which mapped the surface chemical and mineralogical properties of Mercury from 2011-2015.

The MDIS camera and the MASCS spectrometer are the only two instrument suites to have globally mapped Mercury's surface spectral characteristics. MDIS is comprised of two imaging cameras; the Narrow Angle Camera (NAC) that acquired monochrome (0.75 μm) data at a resolution of ~200-500 m/pixel and the Wide Angle Camera (WAC) that acquired global 8-channel multispectral datasets in the spectral range of 0.4-1 μm at the spatial resolution of ~5 km/pixel (Hawkins et al., 2007). MASCS is a hyperspectral point spectrometer suite which consists of a small Cassegrain telescope with an aperture that simultaneously feeds the incoming reflected light from the surface to an Ultraviolet and Visible Spectrometer (UVVS) and a Visible and Infrared Spectro-graph (VIRS). UVVIS mapped the surface at 0.115-0.6 μm at 1 nm spectral resolution. VIRS consists of two separate channels, one in the visible (0.3-1.025 μm) and another in the near-infrared (NIR: 0.95–1.45 μm) that mapped the surface at 5 nm spectral resolution (McClintock and Lankton, 2007). The elliptical orbit and spacecraft pointing constraints resulted in MASCS mapping the surface at dynamically varying spatial resolutions (100m – 7.5km) and high phase angles (>80°); complicating the global hyperspectral characterization of Mercury at a uniform spatial scale.

Global multispectral MDIS data reveals three areally dominant spectral units; low-reflectance material (LRM), moderate-to-high reflectance smooth plains (HRP), and spectrally intermediate terrain (IT) (Robinson et al., 2008). HRP and IT terrains can be identified by a low reflectance, red-sloped, featureless spectrum suggesting the presence of iron-poor silicate minerals, which is supported by ground-based telescope measurements (Izenberg et al., 2014; McCord and Clark, 1979; Vilas et al., 1984; Vilas and McCord, 1976). The absence of a 1-μm crystal-field absorption feature due to ferrous iron in silicates suggests the presence of 0.1-1 wt% of iron in the crustal silicates of Mercury (Murchie et al. 2015; Izenberg et al. 2014; Lucey and Riner, 2011). However, LRM exhibits a 600 nm absorption feature that seems to correlate (Klima et al., 2018; Murchie et al., 2015) with graphite abundance (Patrick N. Peplowski et al., 2016) hinting at a carbon-bearing crust. In addition, the spectra of Mercury's hollows units suggest the presence of sulfides including magnesium-sulfides and calcium-sulfides (Helbert et al., 2013; Vilas et al., 2016).

On the other hand, the geochemistry instrument suite (GRS, XRS, NS) onboard MESSENGER identified nine major geochemical terrains (e.g., Fig. 7a) characterizing the chemical makeup of Mercury's surface (Vander Kaaden et al., 2017). Due to the highly elliptical polar orbit of MESSENGER, the spatial coverage and resolution is highest at the northern hemisphere and that further affects the identification and distribution of these geochemical terrains. These geochemical terranes include: (1) a high-Mg region (HMR); (2) a sub-region of the HMR with the planet's highest Ca and S contents (HMR-CaS); (3) a subset of the northern volcanic plains (NP) with relatively high Mg content (NP-HMg); (4) a subset of the NP with relatively low Mg content (NP-LMg); (5) the Rachmaninoff basin (RB); (6) the planet's largest pyroclastic deposit, located northeast of the Rachmaninoff basin (PD); (7) high-Al regions southwest and southeast of the NP (HAI); (8) the smooth plains within the Caloris basin (CB); and (9) the intermediate terrain (IT), made up of intercrater plains and highly-cratered terrain.

Vander Kaaden et al. (2017) also used the normative mineralogy computation method to derive indirect mineralogy of these geochemical terrains based on the GRS, XRS and NS results and these are tabulated in Table 1.

Namur and Charlier (2017) conducted magma crystallization experiments under reducing Mercury conditions for these geochemically distinct terrains (Peplowski et al., 2015; Vander Kaaden et al., 2017; Weider et al., 2015) to derive a plausible silicate mineralogy for Mercury's surface. Their study found that the oldest volcanic terrains (4.2-4.0 Ga), such as HMR and IT, are dominated by mafic minerals; where HMR is rich in forsterite and IT is comprised of forsterite, plagioclase, and enstatite. However, the youngest lavas (3.9-3.5 Ga), which mostly comprise the IT terrain, are dominated by plagioclase. Namur and Charlier (2017) suggest that Mercury's magma undergoes a temporal evolution where the source of the magma progressively gets shallower and the degree of mantle melting decreases over its geologic history.

Nevertheless, a global mineralogic map of Mercury, which characterizes the different mineralogical properties of the geochemical terrains, has yet to be constructed due to the absence of diagnostic absorption features, such as those attributable to $Fe^{2+}$-poor and Ti-poor minerals. Therefore, the spectroscopic and mineralogical properties of the distinct geochemical terrains on Mercury's surface have yet to be fully characterized.

It is therefore essential to examine the global variation of spectral properties, mainly as a function of geomorphological and geochemical terrains. Spectral analysis from the global coverage of Mercury's surface can characterize the minor variations corresponding to such spectral characteristics as albedo, slope, absorptions, and spectral components indicating the presence of opaques and glasses or space-weathering products.

With the availability of new and revised photometrically calibrated MASCS datasets (PDS MESSENGER Release 16 released on May 12, 2017), it is now possible to conduct global multivariate analysis and derive global spectral parameter maps of Mercury. MASCS higher spectral resolution of 5 nm over more than 185 spectral bands is capable of resolving more subtle spectral variations than the 8-channel MDIS data.

In this study, we present the MASCS global hyperspectral datacube at 1 pixel/degree (42.58 km/pixel spatial resolution at equator) spatial resolution (Section 2). We first examined standard spectral parameter maps, such as the uv-downturn position and the visible spectral slope (Section 3). We then applied an unsupervised clustering algorithm (Section 4.1) and Principal Component Analysis (PCA) (Section 4.2 and Section 5) to further investigate the global spectral heterogeneity across Mercury's surface. Finally, we compare in Section 6 the results obtained from the statistical analysis techniques in relationship to the various geochemical and geomorphological units.

The results and methodology from this study will be useful for analyzing the visible–near-infrared imaging spectrometer (VIHI) datasets of the Spectrometer and Imagers for Mercury Planetary Orbiter (MPO) BepiColombo – Integrated Observatory SYStem (SIMBIO-SYS) onboard ESA/JAXA's BepiColombo mission. The mission launched on October 20, 2018 and is currently enroute to Mercury. VIHI will map the surface mineralogy in the spectral range of 0.4-2μm at a spectral resolution of 6.25nm and a spatial resolution of 100-375m/pixel (Flamini et al., 2010), therefore enabling a higher spatial resolution analysis over a larger spectral range with a higher spectral resolution. In addition, BepiColombo's Mercury Radiometer and Thermal Imaging Spectrometer (MERTIS) will map the surface at a spatial resolution of 500 m/pixel over the 7-14 μm spectral region (Hiesinger and Helbert, 2010). MERTIS observations will provide direct information on the abundance and nature of Si-O

bonds within the bulk silicate mineralogy in addition to characterizing sulfide mineralogies (Maturilli et al., 2017; Varatharajan et al., 2019).

## 2 Creation of Global MASCS hyperspectral cube

For the creation of the global spectral parameter maps, we first prepared a global hyperspectral data-cube image made from the radiometrically calibrated (Holsclaw et al., 2010) and photometrically standardized (Domingue et al., 2019a,b) MASCS VIRS reflectance spectra. We restricted our analysis to the VIS detector observations of the VIRS, because the NIR detector measurements show a lower signal-to-noise (SNR) ratio, which can influence the data classification in an unpredictable manner. To create the global hyperspectral map, we included VIS spectra collected between April 2011 and December 2013 (~4 million spectra)). We excluded data with extreme observing geometries by limiting the observations to those with phase angles less than 85°. A side effect of this data selection is a reduction in the latitudinal coverage to within ±80°N and the exclusion of some off-nadir observations.

MASCS is a point spectrometer with varying field-of-views (FOVs) due to MESSENGER's elliptical orbit and pointing constraints, thereby resulting in spatially varying data coverage. In this study, the data were spatially binned on an equant surface grid in a simple cylindrical projection. We created a global map at 1 pixel/degree spatial resolution (42.58 km/pixel spatial resolution at the equator). This spatial resolution provided the best compromise between coverage, data quality, and computational power needed for the creation of a hyperspectral cube. All spectra in the data cube were resampled to the same 2 nm wavelength resolution ranging from 265 nm to 1015 nm. The median reflectance spectrum of all the data points with their FOV completely within each pixel is calculated for all pixels in the grid. The number of spectral data points for each pixel in the global MASCS cube is shown in Fig. S1 of the supplementary materials.

As a secondary product, we derived a standard deviation hyperspectral data cube for all spectra within a given pixel to use as a measure of data quality, since such a metric can serve as a proxy to monitor sub-pixel variations. The variability map at 700 nm is shown in Fig. S2 of the supplementary materials. These variations are a combination of true variability in spectral properties of the surface within a spatial bin and the measurement uncertainties of the instrument. Fig. S2 shows that only the regions approaching the limiting ±80° latitudes show high variability, due to the highly variable observational geometry in these zones (see, for example, the area at 80°N, 135°W, in Fig. S2).

We further assessed whether the spectral maps were insensitive to variations in temperature of the VIS detector at the time of measurement. Fig. S3 shows the distribution of the VIS detector temperature for all observations used in this study. This distribution does not reproduce any of the features seen in the global maps discussed below or in subsequent spectral classification products, confirming they are not instrumental artifacts.

The hyperspectral datacube obtained by this procedure was visually inspected to check for anomalies, such as those originating from regions with low coverage or from pixels with high sub-pixel variations, and none were found.

## 3 Standard spectral parameter maps

### 3.1 UV downturn

In order to spectrally identify pyroclastic deposits, Goudge et al. (2014) introduced a spectral parameter called the UV downturn. The UV downturn calculates the UV depth of the ratioed reflectance spectra where $UV_{depth} = Depth_{300} + Depth_{325} + Depth_{350}$, as defined in Goudge et al. (2014). In this study we calculated the UV downturn parameter for each pixel of the MASCS global spectral cube (Fig. 1a). As the spatial resolution of the MASCS global spectral cube is very coarse (1 ppd = 42.58 km/pixel at the equator), the UV downturn parameter for the localized, sub-pixel resolution pyroclastic deposits has been overshadowed by the signature of the more abundant surrounding materials. The resulting global UV-downturn map shows no major UV-spectral units.

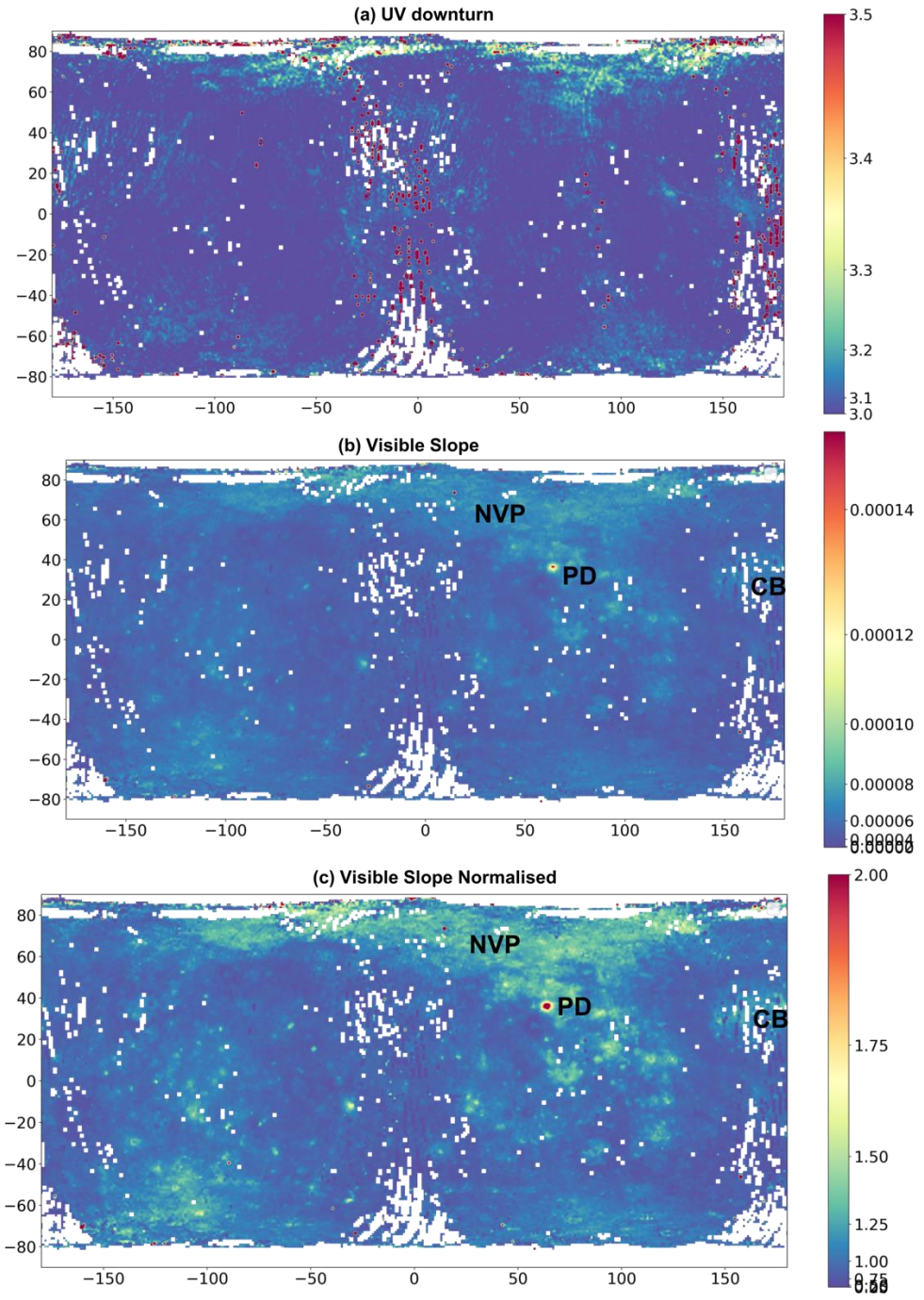


**Figure 1.** Standard spectral parameter maps derived from MASCS hyperspectral data cube. a) UV downturn map is derived using the $UV_{depth}$ from Goudge et al. (2014) and shows at this spatial resolution no major surface units, b) Visible Slope Map is derived using the formula $VIS_{slope} = (R_{550} - R_{750})/(550\text{-}750)$ and c) Normalized visible slope map is the ratio of $VIS_{slope}$ to average Mercury spectrum (Besse et al., 2015; Goudge et al., 2014). Both b) and c) strongly highlight the very bright pyroclastic deposits (PD) located north of Rachmanioff basin as red

units and also reveals the high reflectance northern plains (NVP) and Caloris Basin (CB) as yellow units.

### 3.2 Visible Slope and Normalized Visible Slope

The $VIS_{slope}$ parameter is defined as $VIS_{slope} = (R_{550} - R_{750})/(550\text{-}750)$ (Besse et al., 2015; Goudge et al., 2014) and was computed for each pixel to characterize the global spectral slope properties of Mercury's surface (Fig. 1b). The normalized visible slope map (Fig. 1c) was computed by ratioing the $VIS_{slope}$ values to the average Mercury spectrum derived from the global MASCS data set (Besse et al., 2015). Both of these parameters display very similar variations. However, compared to $VIS_{slope}$ map (Fig. 1b), the normalized VIS slope map strongly highlights some notable spatial units, including the northern smooth plains (NVP-LMg), Nathair Facula (27.5°N 57.4°E), peak-ring basin Eminescu (10.7°N 114.21°E), bright rayed crater Fonteyn (32.8°N 95.5°E), and bright spots within the Caloris basin (30.2°N 162.8°E) (Fig. 1c). Nathair Facula is a prominent volcanic vent located north of Rachmaninoff basin and shows the highest visible slope in the global $VIS_{slope}$ map and also corresponds with the geochemical terrain PD defined by Vander Kaaden et al. (2017).

Therefore, it is safe to say that global visible slope and normalized visible slope maps of Mercury highlight three geochemical terrains, the NVP, CB, and PD. However, these standard spectral parameters are still not efficient to spectrally distinguish, NVP-LMg from NVP-HMg terrains.

## 4 Statistical Analysis Techniques

The MASCS hyperspectral cube used in the multivariate analysis consists of a total of 58493 pixels spreading across the surface at 1 degree/pixel spatial resolution with each pixel consisting of 296 spectral bands in the spectral range of 360 nm to 952 nm at 2 nm spectral resolution. In order to find the global surface spectral variations embedded in the MASCS hyperspectral cube, we applied two multivariate analysis techniques; a) unsupervised clustering analysis (Section 4.1) and b) principal component analysis (PCA) (Section 4.2).

### 4.1 Unsupervised Clustering Analysis

In this study, k-means clustering (MacQueen, 1967), the most widely used unsupervised multivariate partitional clustering algorithm, is used to characterize the global MASCS spectral datacube and identify possible spectral units. K-means is a centroid-based clustering technique, where each spectra (vector) of the datacube is assigned to a specific cluster or central vector. The assignment to a cluster/vector is based by their proximity to the respective cluster/central vector. The parameter k refers to the desired number of clusters. The k-means clustering analysis uses an iterative approach to generate the clusters where the number of iterations is assigned manually.

For a given number of clusters, k, the K-means algorithm randomly chooses k central vectors in B, where B is the number of spectral bands in a MxNxB datacube. The algorithm then iteratively performs the following three steps for the given number of iterations; a) Computes the Euclidean distance between each spectrum in the datacube and the central vector for all k clusters (Bora et al., 2014); b) Each pixel in the image is then assigned to the nearest central vector (cluster); c) Computes new central vectors by calculating the mean vector of all the spectra representing each cluster. The three steps are then repeated for the specified number of iterations. The k central vectors update their definition for each iteration, until they converge to a fixed set of values.

In this study, the initial MxNxB array of MASCS spectral data is 360x180x296 (longitude x latitude x spectral channels), the k-means algorithm then partitions the datacube into a kxB array of cluster centers such that the resulting intra-cluster spectral similarity is high but the inter-cluster similarity is low. The resulting image is an MxN (360x180) array or a 1x1 degree orthogonal map where the values (1,2,..) are the index of the assigned cluster for each pixel. In this study, the value of k is varied from 2 to 20 in steps of 1, and the k-means clustering was performed for each k value (Fig. S4).

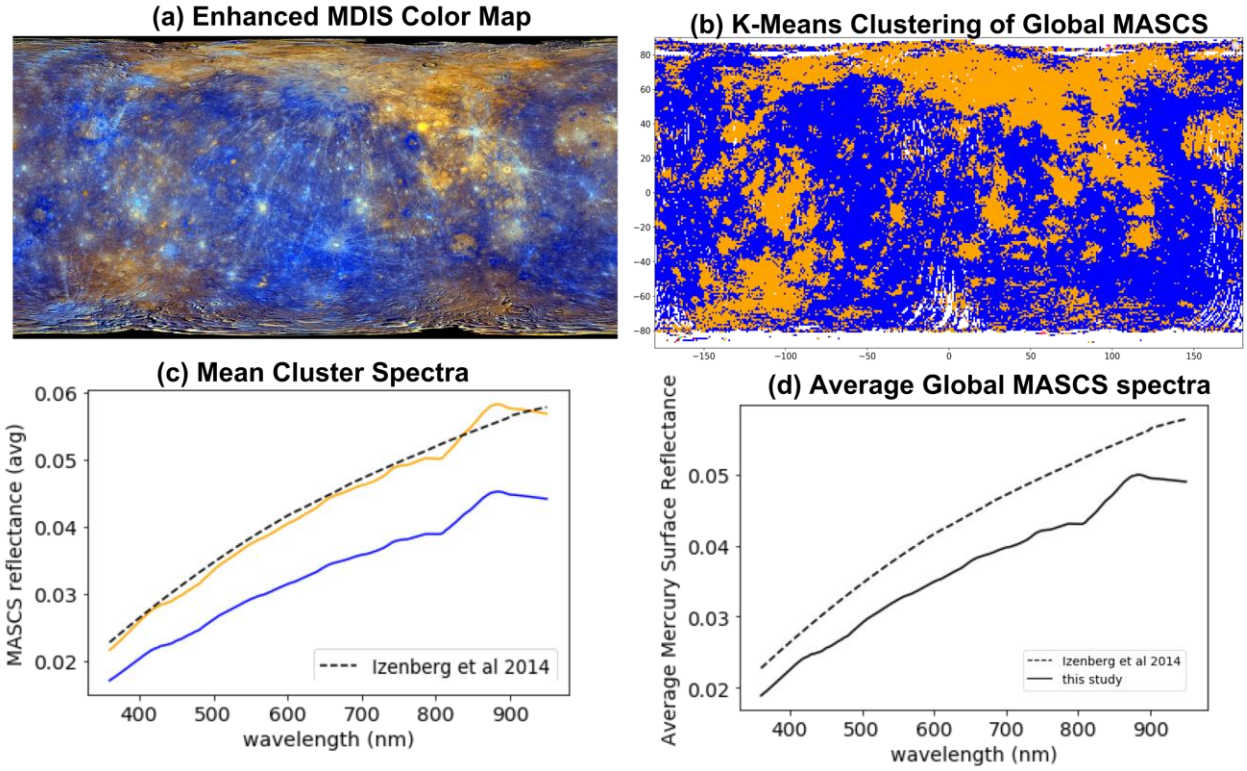


**Figure 2**. a) MDIS enhanced global color mosaic by Domingue et al. (2015), b) K-means clustering of global MASCS datacube for k=2 (orange and blue units) of Mercury, c) shows the mean spectra representing the orange and blue units, d) the new global MASCS average spectra derived in this study. The differences in the global average plotted in (d) is due to the error in the earlier MASCS calibration pipeline which was reported and corrected for the new updated MASCS data products released by PDS.

For each resulting k-means cluster map, the number of pixels per cluster is plotted in Fig. S4. It suggests that irrespective of increased number of clusters (k), most of Mercury's surface falls into two contiguous regions. Figures 2a and 2b compare the MDIS enhanced global color mosaic (Domingue et al., 2015) and the MASCS k-means 2-cluster map, respectively. These figures show a strong correlation between the global MDIS data and the clustered MASCS datacube. The orange units correspond to major geochemical terrains such as NVP, CB, and also include bright rayed fresh craters and volcanic materials within the IT. The blue units however mainly comprise of the underlying material within IT including LRM. This dichotomy in surface spectral properties is also observed in the MDIS enhanced color mosaic (Robinson et al., 2008).

The mean spectra of the corresponding MASCS clusters for the orange and blue units was computed and is plotted in Fig. 2c along with the global average MASCS' spectrum from (Izenberg et al., 2014). It is interesting to note that, the global average used in previous studies actually represents the spectral reflectance of NVP, CB, and lavas within the IT. This is due to an error discovered in the photometric normalization section of the MASCS calibration pipeline (https://pds-geosciences.wustl.edu/missions/messenger/index.htm). This study uses the updated MASCS data products by PDS and the new global average reflectance shows that Mercury surface materials are even darker (Fig. 2d) than reported before.

Fig. 2c shows that among the k-means spectral units, the orange cluster units have slightly redder slope and are brighter than the spectra from the blue cluster units, however, the overall spectral shape between these two clusters is the same.

### 4.2 Principal Component Analysis

In most cases, hyperspectral data (e.g., MASCS) represent more information by preserving the spectral band shape of the minerals; whereas, multispectral data (e.g., MDIS) only contain spectral information from a non-continuous limited number of bands. However, the mean MASCS spectra from the two major clusters resulting from the k-means analysis (Fig. 2c) show that the typical Mercury spectrum is nearly featureless and red-sloped. In this study, we used principal component analysis (PCA), a common multivariate statistical technique, to effectively disentangle the variance among these highly correlated reflectance values for each spectrum in the MASCS datacube (Goodfellow et al., 2016; Jolliffe, 2011). In other words, PCA projects the input vectors (or spectra) composing the datacube into a new orthogonal coordinate system defined by the eigenvectors of the covariance matrix of the original dataset. The first principal component retains the largest variance in the data and the succeeding components represents the highest remaining data variance under the condition that it is orthogonal to the preceding components. Each datapoint of the eigenvector is thus represented by the coefficients relative to each principal component.

In this study, we reduced the 296-channel MASCS datacube to a 9-channel datacube of principal component coefficients. These first 9 coefficients retain 99% of the original variance and are shown in Fig. 3. Fig. 3 (a-i) shows the global principal components PC1, PC2, PC3, PC4, PC5, PC6, PC7, PC8, and PC9 along with their eigen-vectors and are explained below. All the PC maps in Fig. 3 are presented on a uniform scale with values ranging from -5 to 5 and the representative colormap uses a power law scale ($y=x^{\gamma}$, where $\gamma=5$).

a) The PC1 map (Fig. 3a), which represents the highest variance for each MASCS spectra, is similar to the two major clusters obtained from k-means clustering (Fig. 2b) of the MASCS datacube (explained in detail in Section 5.1).

b) The PC2 map (Fig. 3b), which represents the second highest variance and is orthogonal to PC1 map (Fig. 3a), interestingly displays similar clusters as the k-means clustering (Fig. 2b), but the inverse of what is seen in the PC1 map. The spectral significance of PC2 map is explained in detail in Section 5.2.

c) The PC3 (Fig. 3c), PC4 (Fig. 3d), and PC5 (Fig. 3e) maps show no significant correlation with surface units, displaying little spatial variance among these principal components.

d) PC6 (Fig. 3f) shows localized spectral units that represent specific surface characteristics and its discussed in detail in Section 5.3.

e) PC7 (Fig. 3g), PC8 (Fig. 3h), and PC9 (Fig. 3i) also show no significant correlation with surface regions and may correspond to the noise in the data from spectra of the high northern and southern latitudes.

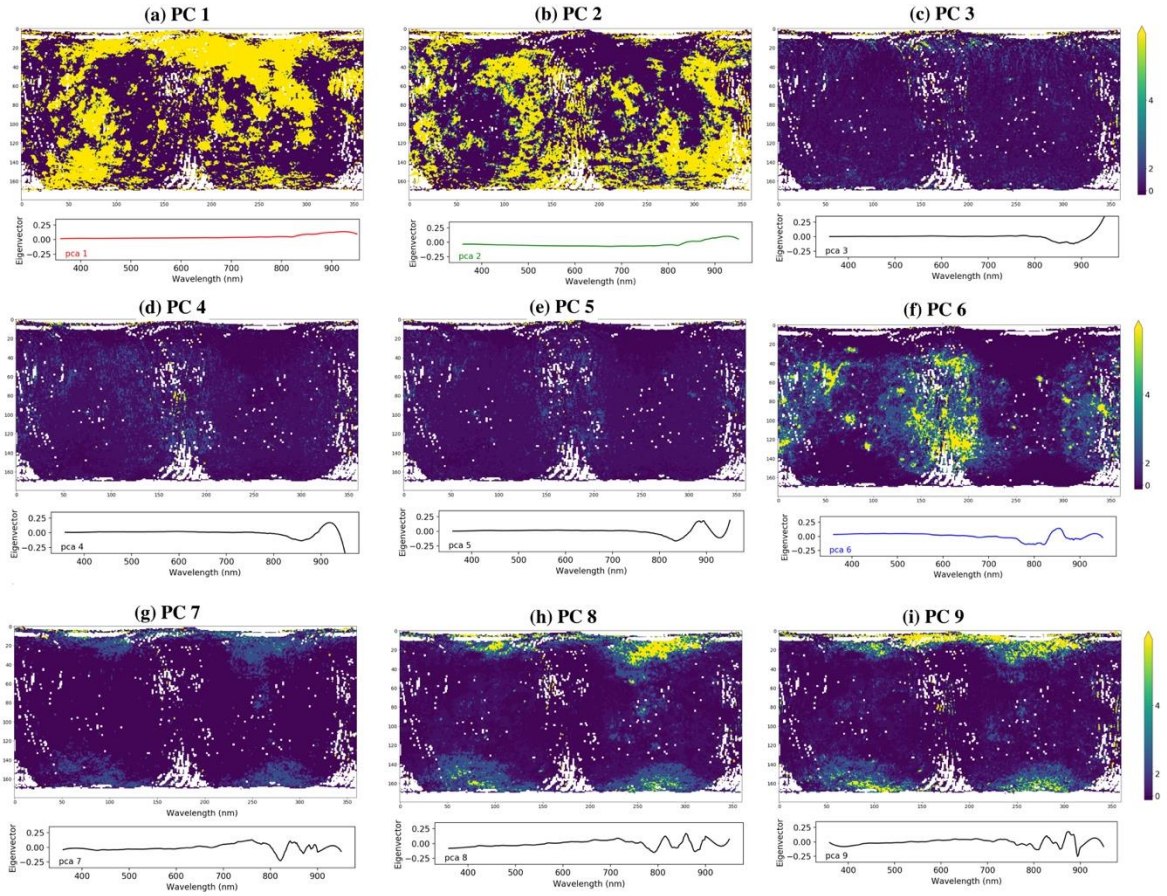


**Figure 3**. (a-i) Top box of each panel shows the PCA coefficients maps for components PC1 to PC9 respectively represented by a uniform scale with values ranging from -5 to 5 and the representative colormap uses a power law scale ($y=x^{\gamma}$, where $\gamma=5$). Bottom box: shows the corresponding eigen vector of each principal component. PC1 and PC2 are orthogonal to each other and further representing two contiguous spectral clusters as K-Means map (Fig. 2b). PC6 shows localized spectral units that represent specific surface characteristics (see Fig. 6) and discussed in detail Section 5. The rest of the PCs show no significant correlation with surface units, displaying little spatial variance among these principal components.

## 5 Regional and Global perspective of MASCS primary PCs

As discussed in Section 4.2, MASCS PCA analysis reveals three primary principal component coefficients, PC1, PC2, and PC6 (Fig. 3), that correlate with geomorphologically and geochemically distinct terrains on Mercury. The significance of these primary PCs is discussed below.

### 5.1 Principal Component (#1)

The MASCS PC1 map (Fig. 4) is closely associated with the global reflectance map at 750 nm. For example, the PC1 values corresponding to yellow pixels in Fig. 4a (PC1) closely

resembles the global reflectance (at 750 nm) map (Fig. 4b), suggesting brighter surface materials with albedo ~>0.05 at 750 nm are distinguished by PC1. The PC1 map also strongly resembles the global k-means cluster map of Mercury (Fig. 2b; Section 4.1). Notable geochemical terrains associated with this component includes the northern volcanic plains (NVP), Caloris basin's (CB) interior, and pyroclastic deposits (PD). This suggests that PC1 may be correlated with younger Mercury terrains which include volcanic plains, fresh impact crater units, bright pyroclastic deposits, and fresh bright hollows.

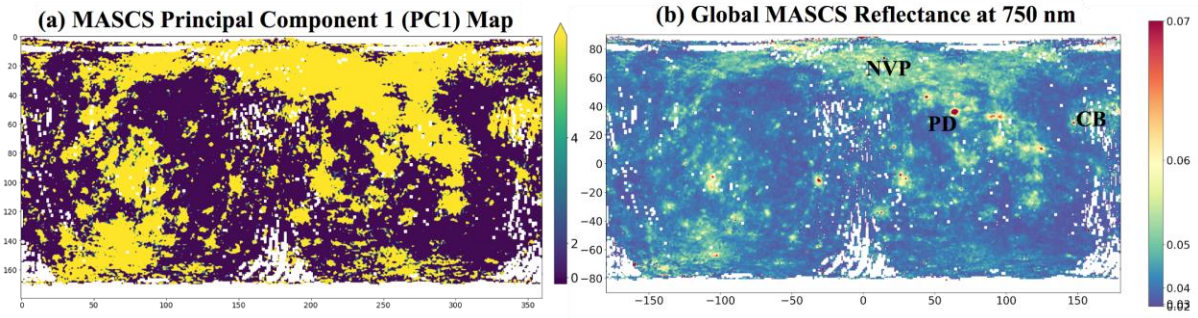


**Figure 4**. a) PC1 map represents the highest variance for each MASCS spectra and is similar to the two major clusters obtained from k-means clustering (Fig. 2b) b) Global MASCS reflectance at 750 nm highlighting three major geochemical terrains which includes northern volcanic plains (NVP), caloris basin (CB), and pyroclastic deposits of Nathair Facula (PD). Comparsion of a) and b) shows that the yellow units in PC1 map represents the surface with reflectance value ~>0.05 at 750 nm.

### 5.2 Principal Component (#2)

In contrast to PC1, PC2 correlates with darker underlying materials, representing the oldest terrains (>4 Ga) on Mercury (Fig. 5a). Comparisons of the PC2 map with the derived space weathering map (Fig. 5b) of Trang et al (2017), show correlations with weathered units with abundances of nanophase iron >1.167%, as derived by Trang et al. (2017) from the MASCS VIRS data. This suggests that, PC2 seems to be correlated with older Mercury terrains which include intermediate terrains (IT), LRM units, and Caloris exterior smooth plains.

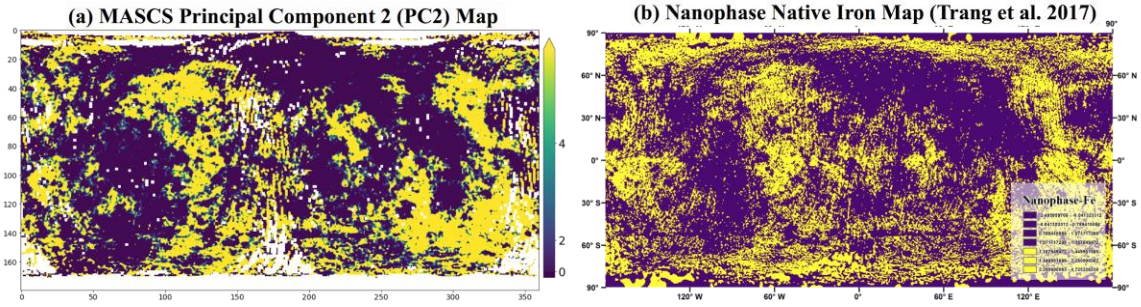


**Figure 5**. a) PC2 map represents the second highest variance for each MASCS spectra and is orthogonal to PC1 map as shown in Fig. 4a and b) nanophase iron map from Trang et al. (2017). The comparison between a) and b) shows that yellow units represented by PC2 map closely relates to the surface materials with higher degree of space weathering.

### 5.3 Principal Component (#6)

The PC6 map is in Fig. 6 overlaid on the MDIS color basemap to better understand the spectral surface characteristic represented by this particular principal component. Comparisons of the PC1 map (Fig. 4a) and the PC6 map (Fig. 6a) show that the PC6 represents units that are a subset of those represented by PC1. A few of the surface features represented by PC6 are discussed below (Fig. 6b-k). Using the MDIS color basemap, the bright and dark surface features highlighted by yellow regions of PC6 map are marked in white and black arrows respectively in the figures 6b-k (left). Within the PC6 map (Fig. 6a-k), the blue regions generally surround the yellow regions and the violet units have the lowest PC6 values.

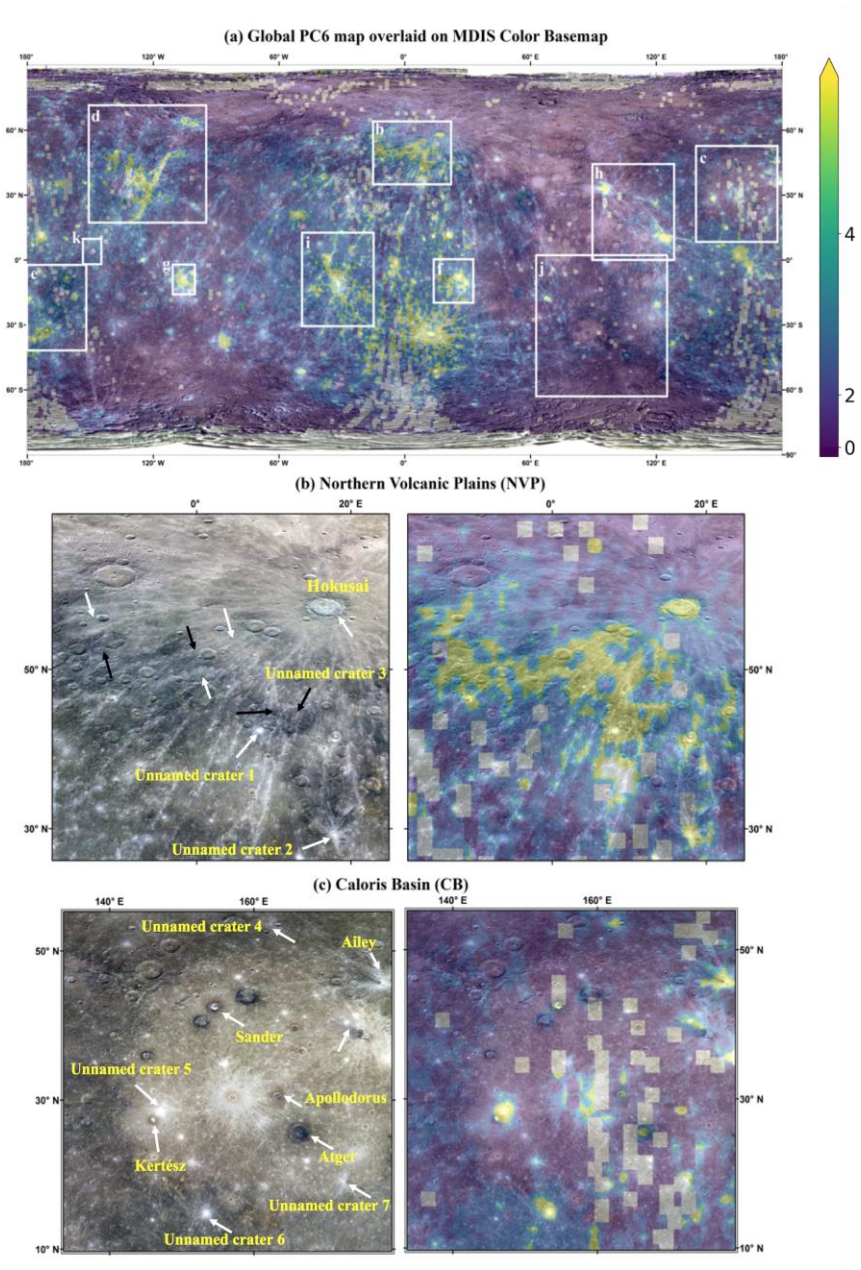

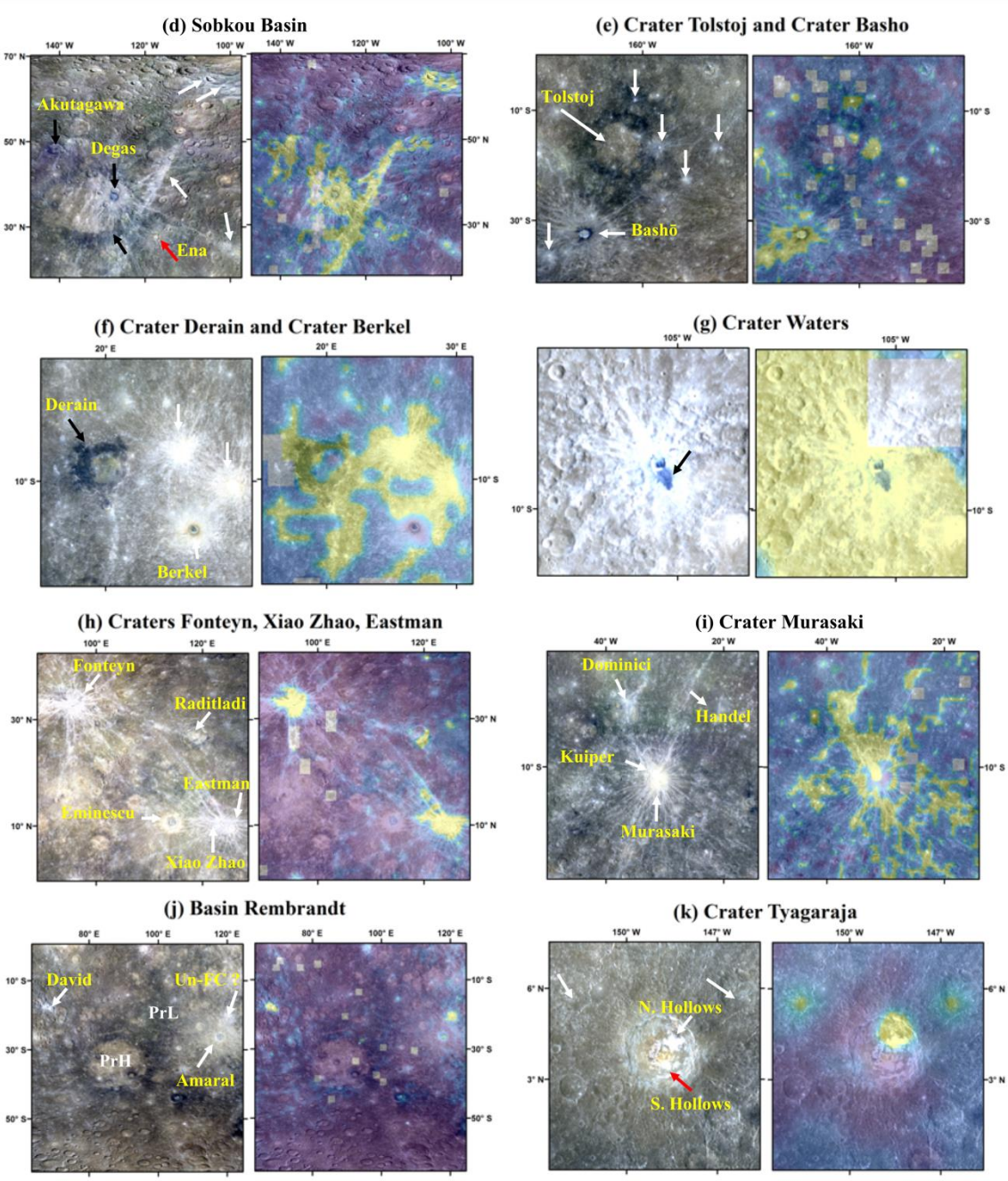


**Figure 6**. a) PC6 map is overlaid on the MDIS 8-color basemap and the white boxes corresponds to study regions shown in b) northern volcanic plains, c) Caloris basin, d) Sobkou basin, e) craters Tolstoj and Basho, f) craters Derain and Berkel, g) crater Waters, h) craters Fonteyn, Xiao Zhao, and Eastman, i) crater Murasaki, j) basin Rembrandt, and k) crater Tyagaraja. Left images in b-k corresponds to MDIS color basemap of each study region and those on the right to its corresponding PC6 map. The white and black arrows in each MDIS color map in b-k corresponds to the bright and dark surface units respectively those belong to yellow regions in PC6 map (b-k; right).

**Northern Volcanic Plains (NVP, Fig. 6b):** The NVP are the largest smooth plains unit on Mercury, hosting two geochemical regions; a) a low-Mg terrain (NVP-LMg) that covers most of Borealis planitia, and b) a high-Mg terrain (NVP-HMg) that extends over a smaller portion of the NVP to the south of the crater Hokusai (D=114 km, 57.86ºN 16.63ºE) (Vander Kaaden et al., 2017). Within the NVP, PC6 highlights surface materials within the NVP-HMg regions, which include both brighter (white arrows) and darker (black arrows) materials seen in the MDIS color map. Morphologically, there are no clear borders that distinguish the PC6 units from rest of the NVP. The brighter PC6 units include the rim and floor of Hokusai crater and a portion of its ejecta rays, two fresh bright-rayed unnamed craters (labeled unnamed crater 1 & unnamed crater 2 in Fig. 6b left). Some of the darker materials highlighted by PC6 include darker plains in the north of unnamed crater 1 and the northern crater wall and floor of unnamed crater 3 (Fig. 6b left), possibly contaminated with brighter ejecta materials from nearby fresh craters.

**Caloris Basin (CB, Fig. 6c):** Caloris is the youngest and largest impact basin (D=~1550 km, 31.84ºN 162.45ºE) on Mercury, preserving the post-volcanically and -tectonically modified landforms within its interior HRP (Murchie et al., 2008). Associated with Caloris is the presence of a radial magnetic anomaly (Hood, 2016). Caloris planitia also hosts craters, such as Sander (D = 47 km, centered at 42.44ºN 154.60ºE) and Kertész (D = 32 km, centered at 27.40ºN 146.10ºE), which contain hollows units within their LRM floors. The hollows units have been shown to host volatile-rich materials (Blewett et al. 2013, Helbert et al. 2013, Vilas et al. 2016). Along the entire CB floor, the PC6 units correlate only with brighter surface features, such as bright rayed fresh/immature craters (for example crater Ailey (D = 23 km, centered at 45.58ºN 177.93ºE)), the hollow materials within craters Kertész and Sander, and the bright central peaks of craters Atget (D = 100 km, centered at 25.58ºN 166.37ºE) and Apollodorus (D = 41.5 km, centered at 30.55ºN 163.39ºE). The Caloris basin interior smooth plains (HRP) and the LRM units within such craters as Munch (D = 57 km, centered at 40.46ºN 152.75ºE) and Poe (D = 77 km, centered at 43.76ºN 159.09ºE) are not correlated with PC6. Examination of the PC6 map within Caloris basin (Fig. 6c) suggests that irrespective of the differences in the compositions among the varying morphologies (hollows, fresh craters, central peaks) correlated to this principle component, the PC6 units may only highlight materials (yellow units) which are relatively fresh or immature.

**Sobkou Basin (Fig. 6d):** The ~>4.0 Gy old Sobkou Basin (D=770km; 35◦N 225◦E) lies in Sobkou Planitia which is associated with two magnetic anomalies (Hood, 2016). It possesses a stronger magnetic anomaly that is correlated with surrounding dark LRM ejecta materials, and a weaker magnetic anomaly within the basin floor HRP materials that are volcanic in origin (Hood, 2016). Within Sobkou planitia lies the Degas crater (D=45 km). Degas is one of the freshest bright-rayed craters on Mercury's surface. It is surrounded by LRM along its rim and contains bright hollows within its crater floor (Blewett et al., 2013; Bott et al., 2019; Thomas et al., 2014). PC6 (Fig. 6d) correlates with the brighter materials within Degas crater and with the crater's ejecta, including the darker rim. PC6 (Fig. 6d) also correlates with regions of darker albedo materials, such as the rim of Akutagawa (D=106 km 48.25ºN 141.03ºW) crater, in addition to other brighter albedo regions such as the bright ejecta streak on the eastern rim of the older basin in Sobkou planitia. Like CB, PC6 units within Sobkou planitia highlight compositionally different surface units.

**Tolstoj Basin and Basho Crater (Fig. 6e):** Tolstoj (D=355 km, 16.2◦S 165◦W) is a ~3.9-4.0 Gy old basin characterized by LRM-rich ejecta and a basin floor filled with HRP volcanic plains, and is thus one of the highest color contrasting features on Mercury's surface

(Robinson et al., 2008). In contrast, Basho crater (D=64 km, 32.4°S 170.5°W), located south-west of Tolstoj, has bright-rayed ejecta and a dark, LRM-containing rim, thus exposing compositionally heterogeneous upper crustal materials (Robinson et al., 2008). In the PC6 map (Fig. 6e), the Tolstoj region, including both the LRM and HRP materials, show no correlation with even the lowest PC6 values. On the other hand, the LRM rim, bright crater floor, and bright ejecta materials from the younger crater Basho, are strongly correlated to PC6. The white arrows in Fig. 6e indicate additional small fresh/immature craters which both expose brighter materials and are strongly correlated with PC6.

**Derain and Berkel Craters (Fig. 6f):** Derain crater (D=175 km; 9°S, 19.7°E) is a pit-floored "unfilled" crater formed between the Mansurian (~3-3.5 Ga) and Tolstojan (~3.9-4.0 Ga) eras (Hargitai et al.; Herrick et al., 2018). It is well known for the presence of an asymmetric annular distribution of LRM along its rim (Denevi et al., 2009; Mancinelli et al., 2015; Xiao et al., 2013) and shallow pits with irregular and scalloped walls which conform to its central peak. Intriguingly, the PC6 component within this crater correlates only with the LRM material covering the crater rim. Also noted in the PC6 map of this region is a correlation of this component with another asymmetric dark-rayed fresh crater (D = 21.28 km; 11.9°S, 20.1°E) south of Derain (marked by a black arrow in Fig. 6f).

Like the LRM discussed above, the fresh material excavated by two bright-rayed craters, un-fc1 (D= <166m, 8.19°S, 25.75°E) and un-fc2 (D=27.7km, 10.32°S, 29.83°E) (marked by white arrows in Fig. 6f) are also correlated with PC6 (Fig. 6f). However, the dark crater floor and the bright ejecta of Berkel crater (D=23 km, 13.7ºS 26.8ºE) within this same region shows no correlations in the PC6 map. Independent of the heterogeneity in the composition, depth, freshness of the excavated material, and the close proximity of these craters, the higher PC6 values (yellow pixels) indicate a similar physical structure for these diverse surface materials, possibly an indicator of a fine-grained component to the surface regolith in these regions.

**Waters Crater (Fig. 6g):** Waters crater is a geologically young, 15 km diameter, bright-rayed, fresh crater (centered at 8.96°S 105.45°W) that possess a 20 km long, dark impact-melt flow feature (Blewett et al., 2014; D'Incecco et al., 2015), which is indicated by the black arrow in Fig. 6g. Within this spatial scale both Waters crater and the melt-flow are contained in the same spatial pixel; however, this is the very important target for the high spatial resolution data. The phase-ratio analysis of Waters crater suggests that this particular low reflectance melt-flow has a different photometric character than the surrounding terrains (Blewett et al. 2014). The melt-flow displays an increase in reflectance with decreasing phase angle; suggesting that the melt-flow is comprised of coarse-grained regolith compared to the finer-grained regolith in the surrounding units. D'Incecco et al. (2015) suggests that the color differences between the crater and its melt-flow could also be explained by compositional heterogeneities, shock metamorphism, and/or space weathering effects. However, the PC6 map displays no differences between the crater, its ejecta, and the melt-flow. This may be due to the low spatial resolution of global MASCS data (42.58 km/pixel).

**Raditladi Region (Fig. 6h):** The region covered in Fig. 6h is known for the presence of hollows within the peak-ring and floor of Raditladi basin (D=258 km, 27.17ºN 119.12ºE) and within the central peak and peak-rings of Eminescu crater (D=129 km, 10.66ºN 114.19ºE) (Blewett et al., 2011). The PC6 map displays correlations only with the fresh hollow materials exposed in the south-eastern peak ring of Raditladi basin. The hollows within the peak-rings of Eminescu are not seen in the PC6 map, which could be due to the coarse spatial resolution of the MASCS spectral datacube. The two bright rayed fresh craters Fonteyn (D=29 km, 32.82ºN

95.52ºE) and Xiao Zhao (D=24 km, 10.59ºN 123.79ºE), along with their ejecta rays, are distinguishable in the PC6 map. This suggests that irrespective of compositional differences, for example hollows or crustal material, it is the immature nature of the surface regolith that is highlighted in the PC6 map.

**Kuiper and Murasaki Craters (Fig. 6i):** Kuiper (D=62 km, 11°S, 31.5°W) is one of the brightest Mercurian features, possessing prominent bright ejecta-rays. It sits on the north-western topographic rim of the older and more degraded Murasaki crater (D=132 km, 12.5°S, 30.4°W) (De Hon et al., 1981; Hapke et al., 1975; Harmon et al., 2007, D'Incecco 2015). Kuiper marks the beginning of the youngest chronostratigraphic period on Mercury (~1 Ga; Kuperian) (Spudis and Guest, 1988). Mariner 10 data suggests the excavation of material with a low-opaque content for both Kuiper and Murasaki (Robinson and Lucey, 1997; Blewett et al., 2007; Blewett et al., 2009). In the PC6 map (Fig. 6i), the ejecta rays of both young Kuiper and older Murasaki display a strong correlation to PC6. The PC6 map also shows a correlation between PC6 and Dominici crater (D=20 km, 1.38°N 323.5°E). A 629 nm absorption feature detected in the MDIS color data (Vilas et al., 2016) suggest the presence of sulfides (CaS, MgS) in the fresh hollows on Dominici's southern rim/wall. Overall, in Fig. 6i, the PC6 map suggests correlations between PC6 and surfaces hosting immature and/or low-opaque materials.

**Rembrandt Basin (Fig. 6j):** Rembrandt is the second largest impact basin after Caloris and is one of the youngest impact basins, with a similar age to Caloris basin (~3.9 Ga) (Watters et al., 2009). This ~715 km diameter basin (32.9°S 87.9°E) impact event led to the formation of two spectrally and morphologically distinct units; a) a rough textured impact melt deposit identified by low-reflectance exterior plains (PrL) and b) a smooth textured volcanic infilling identified by high-reflectance interior smooth plains, which formed in quick succession with the basin formation (Whitten and Head, 2015). Therefore, the PC6 map does not display any correlation with either of the spectrally distinct units within Rembrandt basin.

Also, within the region shown in Fig. 6j is the bright-rayed, ringed-peak cluster basin Amaral (D=105 km, 26.5°S 117.8°E), which is Kuiperian in age (~1 Ga) (Kinczyk et al., 2016). There are varying correlations within this basin that are distinguishable in the PC6 map, with the ringed-peak clusters having the strongest correlation. Spatially resolvable are fresh bright-rayed craters such as David (D=23 km, 17.7°S 67.9°E) and an unnamed fresh crater (D=17.25 km, 20.4°S 120.6°E); both showing strong signatures in the PC6 map. This suggests that irrespective of the type of composition (volcanic or crustal), the PC6 component highlights the physical properties of the surface, especially those containing very fresh material identifying regions which have experienced the least amount of regolith processing.

**Tyagaraja Crater (Fig. 6k):** Tyagaraja crater (D=97 km, 3.9°N 148.9°W), formed in the Mansurian (~3.0-3.5 Ga) to Kuiperian (~1.0 Ga) period (Jozwiak et al., 2018; Kinczyk et al., 2016), is well known for having excavated subsurface LRM. This crater also contains extensive bright-halo hollows (N. hollows and S. hollows; Fig. 6k) on its crater floor alongside probable pyroclastic vents (Blewett et al., 2011). In the PC6 map, the regions covering the north-eastern crater rim, wall, and the floor covering part of the N. Hollows are distinguishable. The remainder of the crater, including the pyroclastic vents and the S. Hollows are not distinguishable in the PC6 map due to the coarser spatial resolution. The PC6 map also correlates with two areas on either side of the northern region of the crater; however, morphologically, these two areas are not correlated to any unique morphologically or geochemically distinct units.

## 6 Global Multivariate Spectral Analysis

In this study, we created a global MASCS false color composite (FCC) map using PC1, PC2, and PC6, where each component was assigned to a color channel (red, green, and blue, respectively, Fig. 7a) to understand the spectral heterogeneity of the Mercury surface and its relation to Mercury's geochemistry and mineralogy. The boundaries of the geochemical terrains found by Vander Kaaden et al. (2017) are overlaid on the FCC (Fig.7a, black) to examine any correlations between the geochemical terrians and the MASCS spectral units. The white boxes in Fig. 7a corresponds to the PC6 study regions discussed in Section 5.3. The MASCS' FCC map was then overlaid on the MDIS 3-color (R: 1000nm, G: 750nm, B: 430nm) global map (665 m/pixel spatial resolution) for a comparative analysis of the spectral and color terrains of Mercury, shown in Fig. 8. Table 1 summarizes the MASCS PC color units from Fig. 7a and its corresponding derived mineralogy from Namur and Charlier, (2017) and Vander Kaaden et al. (2017) for each geochemical terrain which are further discussed in Section 6.1.

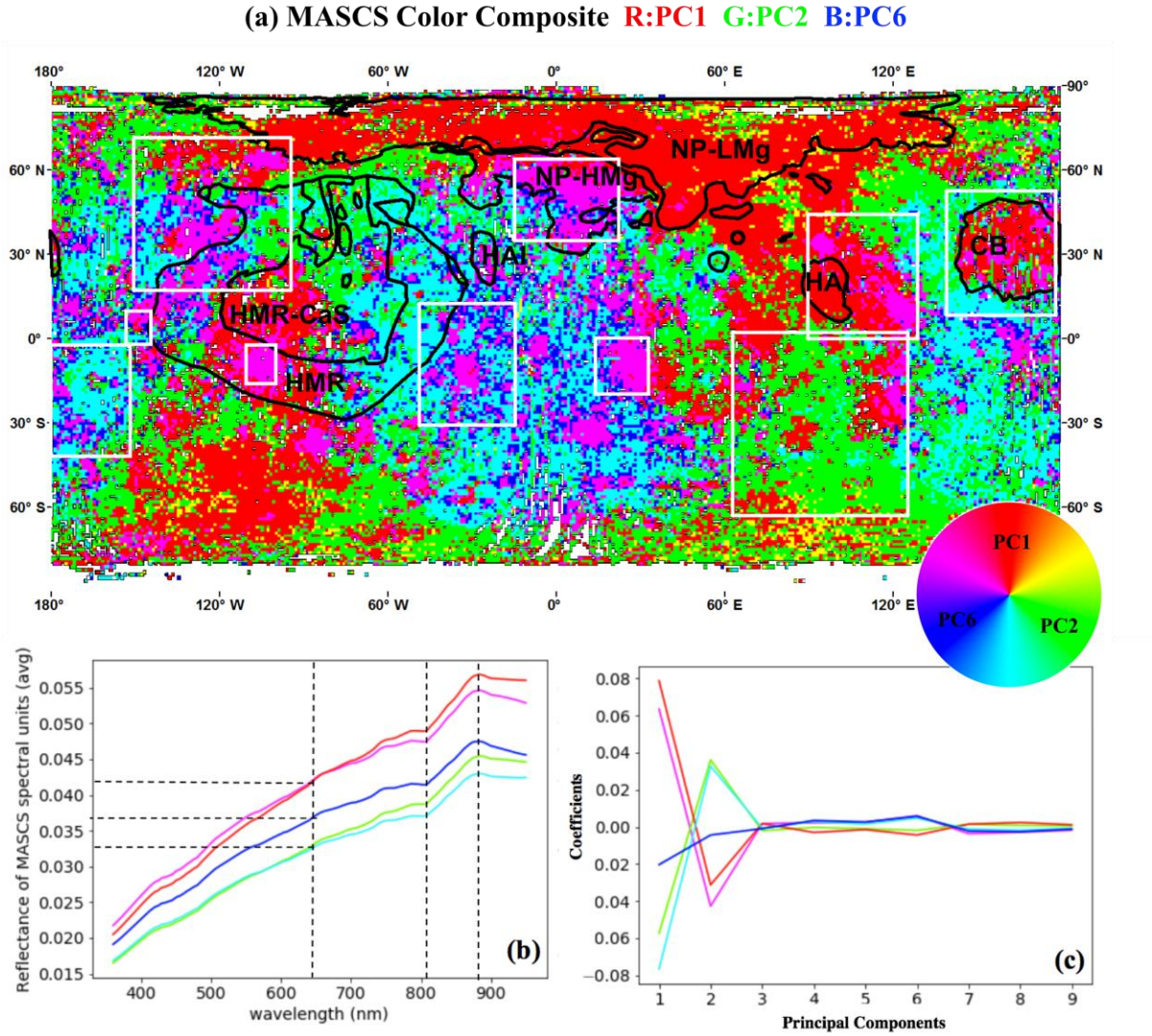


**Figure 7.** a) MASCS false color composite (FCC) map created by assigning red, green, and blue channels to PC1, PC2, and PC6 respectively. MASCS FCC shows that Mercury's

surface can be broadly characterized into 5 color units; red, green, pink, cyan, and blue. The white boxes correspond to the study regions mapped in PC6 map, shown in Fig. 6a, where the pink units within the white boxes correspond to the yellow units in PC6 map in Fig. 6a. The black boundaries correspond to various geochemical terrains mapped by Vander Kaaden et al. (2017). The northern volcanic plains having high-Mg (NVP-HMg) and low-Mg (NVP-LMg) are characterized as two distinct spectral units, pink and red respectively, in MASCS FCC. b) the average spectra of each color units in FCC. The vertical dotted line along 650 nm is used to classify these color units: high reflectance units (red, pink), low reflectance units (green, cyan), and intermediate reflectance units (blue). The intermediate reflectance units generally envelope the pink units. The average spectra of all color units display two minor absorption features near ~450 nm and ~800 nm along with a downward slope after ~890 nm. c) the plot between each principal component and the coefficients of each color unit.

The global MASCS PC color composite shown in Fig. 7a can be visually characterized by five distinct color units:

a) red units correspond to spatial regions belonging to the highest values (yellow regions) in the PC1 map (Fig. 4a), and lowest values (violet regions) in the PC2 (Fig. 5a) and PC6 (Fig. 6a) maps (PC1>>PC2~PC6).

b) green units correspond to spatial regions belonging to the highest values (yellow regions) in the PC2 map (Fig. 5a), and lowest values (violet regions) in the PC1 (Fig. 4a) and PC6 (Fig. 6a) maps (PC2 >> PC1~PC6).

c) pink units correspond to common areas within the yellow regions in the PC1 map (Fig. 4a) and PC6 map (Fig. 6a) respectively (PC1~PC6 >> PC2). All the pink regions within the white boxes in Fig. 7a correlates with the yellow regions in PC6 map in Fig. 6a.

d) cyan units correspond to common areas within the yellow regions in the PC2 map (Fig. 5a) and intermediate values (blue regions) in PC6 map (Fig. 6a) respectively (PC2~PC6 >> PC1).

e) blue units don't share any common properties of PC1 and PC2 and commonly surrounds pink and cyan units (PC6 >> PC1~PC2).

From the context of Mercury's surface as characterized by the PC1, PC2, and PC6 components (discussed in Section 5), the five distinct color units in the MASCS' FCC map segregate Mercury's surface into; 1) red units; high reflectance spectral units (HRPs) mainly representing young volcanic smooth plains, including the northern smooth plains and the Caloris interior plains, 2) pink units; representing some of the younger and immature surface regolith typically believed to contain low-opaque materials and have experienced the minimum amount of space weathering (such as hollows, fresh bright-ejecta craters, brighter peak rings, and some of the exposed LRM units), 3) green units; representing some of the oldest terrains such as dark, LRM-containing surface materials, 4) cyan units; generally representing darker LRM terrains contaminated by ejecta from surrounding young craters, and 5) blue units; commonly surrounding both pink and cyan units.

For each of these five color units, the corresponding average spectra and their coefficients of nine principal components are shown in Fig. 7b and Fig. 7c, respectively. In terms of spectral shape (Fig. 7b), all five of the color units from the MASCS' FCC map (Fig. 7a) display a positive spectral slope with two minor absorption features; one near ~450 nm and another near ~800 nm, with a downward slope after ~890 nm. In terms of MASCS' spectral reflectance at

~650 nm, Mercury's surface can be broadly divided into three spectral clusters (highest-intermediate-lowest reflectance units):

1) red and pink units with 650 nm reflectance values of ~0.0425 (highest). The overall spectra of the pink units display a slightly shallower slope compared to the red units.

2) blue units with 650 nm reflectance values of ~0.0375 (intermediate)

3) green and cyan units 650 nm reflectance values of ~0.0325 (lowest). Spectrally, the slope and the reflectance value of the cyan units are similar to the green units up to ~650 nm, and afterwards the spectral slope decreases in comparison.

The average coefficient values of nine principal components representing each color unit in the MASCS PC color composite are plotted in Fig. 7c, clearly revealing these three families of spectral units across Mercury's surface.

### 6.1 Comparative Analysis of MASCS-derived Spectroscopy, Mineralogy, and Morphology of various Geochemical Terrains of Mercury

The MASCS derived spectral nature of the geochemical terrains on Mercury and its context to inferred surface mineralogy is discussed in detail in the following sub-sections. The mineralogy derived from the geochemical observations are summarized in Table 1. The following sub-sections discuss the spectral nature of the major geochemical terranes with respect to their representative color units in the MASCS color composite map (Fig. 7a, Table 1).

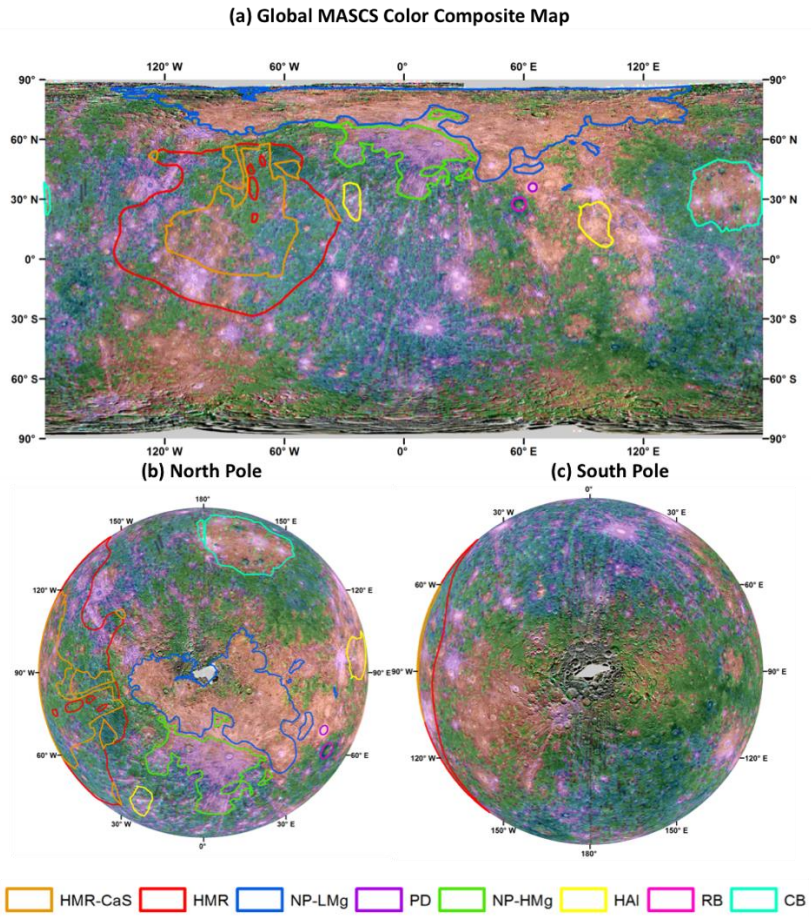

**Figure 8.** a) Global MASCS False Color Composite Map shown in Fig. 7a along with the boundaries of nine geochemical terrains defined by Vander Kaaden et al. (2015) overlaid on the MDIS color basemap. b) and c) corresponds to the north and south polar stereographic projection of (a) respectively.

**Table 1. Comparative analysis of spectral, inferred mineralogical and geochemical units of Mercury from MESSENGER datasets**

| Geochemical Terranes[a] | *MASCS PC Color units | (Experimental) Silicate Mineralogy[b] | | | | | Normative Mineralogy[a] in wt% | | | |
|---|---|---|---|---|---|---|---|---|---|---|
| | | volcanic | Basement (%) | | | | Plg | Dominant pyx | Ol | sulfides |
| | | | Plg | Fo | Di | En | | | | |
| NVP-LMg | | dominantly Plg in addition to Fo and Di | >50 | 10-15 | >15 | - | >50 | Hyp+**Diop** | <2 | ~4 |
| NVP-HMg | | | | | | | <50 | Hyp | ~11 | ~4 |
| HMR | | May contain only Fo crystals | <40 | >25 | >20 | <15 | <50 | **Diop** | ~27 | >5 |
| HMR-CaS | | - | - | | | | <50 | **Diop** | >30 | ~6.25 |
| IT | | Fo or Fo+Di | >45 | - | - | >25 | >50 | Hyp | <2 | ~4 |
| CB | | - | >60 | sub-equal amounts | | | >50 | Hyp | - | ~3.14 |
| RB | | NA | NA | | | | <50 | **Diop** | ~24 | >5 |
| PD | | NA | NA | | | | <50 | **Diop** | ~29 | ~1.56 |
| HAI – West | | NA | NA | | | | >50 | Hyp | - | ~4 |
| HAI – East | | NA | NA | | | | | | | |

*Correlation of MASCS PC color units; red (PC1>>PC2~PC6); pink (PC1~PC6 >> PC2); green (PC2 >> PC1~PC6); cyan (PC2~PC6 >> PC1); blue (PC6 >> PC1~PC2) (See Section 6)

[a]Geochemical terranes of Mercury surface and its normative mineralogy [*Vander Kaaden et al.*, 2017]. Range of Plg is 37.52 % (HMR-CaS) – 58.35 % (NP-LMg)

[b]Silicate mineralogy derived from geochemistry laboratory experiments [*Namur and Charlier*, 2017]

### 6.1.1 One color units: NVP, RB, PD, HAI-East

The geochemical terrains NVP-LMg, NVP-HMg, RB, PD, and HAI-East each display homogeneous spectral characteristics in the MASCS color composite map (Fig. 7a; Table 1). Among them, NVP is the largest volcanic plains unit on Mercury; hosting two categories of volcanic units: NVP-LMg and NVP-HMg. These two volcanic units are distinguished purely by the amount of Mg in their chemical composition (Vander Kaaden et al., 2017). In the MASCS FCC map (Fig. 7a, 8a), the NVP-LMg and NVP-HMg terrains are uniquely characterized by two discrete spectral units, the red and pink units that share boundaries with these geochemical terrains (Vander Kaaden et al., 2017). However, these two terrains are not discernable in the global MDIS color composite map (Denevi et al., 2013; Domingue et al., 2011; Domingue et al., 2015). Vander Kaaden et al. (2017) suggest that the NVP-HMg composition is characterized by a higher presence of orthopyroxenes and olivines than the NVP-LMg (Table 1). Spectrally, these two terrains share similar shape and reflectance at 650 nm, however, the slope of the NVP-HMg (pink) is slightly lower compared to NVP-LMg (red) (Fig. 7b) consistent with the compositional difference proposed by Vander Kaaden et al. (2017).

Geochemically, RB and PD share roughly similar inferred silicate mineralogies with plagioclase, diopside, and olivine, however they differ in the abundance of sulfides (Table 1). RB is a ~3.6 Ga old basin (D=305 km, centered 27.39°N 58.56°E) hosting some of the youngest lava flows on Mercury (Marchi et al., 2011). PD is located NE of RB and contains some of the brightest and largest pyroclastic deposits, which are associated with Nathair Facula (centered 35.97°N 65.47°E). At this spatial resolution in the MASCS FCC map (Fig. 7a), PD displays a red color similar to the NVP-LMg region while RB displays a green color associated with PC2, that represents space-weathered, older Mercury terrains. Spectrally, PD and RB terrains represent the two extreme spectral unit endmembers, highest and lowest 650 nm spectral reflectance, respectively (Fig. 7b; red, green). On the other hand, HAI in the eastern longitude (HAI-East) shares similar MASCS color characteristics as PD (red), however, HAI differs significantly in its derived mineralogy, as it is associated with the absence of olivines and comparatively greater amounts of sulfides (Table 1).

### 6.1.2 Two-color units: CB, HAI-West

Geochemically, CB and HAI-West have very similar inferred mineralogies; with plagioclase, clinopyroxenes, 3-4 wt% sulfides, and no olivine component (Table 1). However, in the MASCS FCC map (Fig. 7a, 8a; Table 1), CB and HAI-west are dominated by red and pink units, respectively. This suggests that PC1 is a major spectral component for both CB and HAI-west regions, as is also apparent for the HAI-east region (see section 6.1; Table 1). Within CB (Fig. 8a), the bright-rayed ejecta craters and fresh bright hollow materials are displayed as pink units whereas dark-floor crater Atget is displayed as a cyan unit due to contributions from PC6 (see section 5.3; Fig. 6c). However, in the case of HAI-west, there are no clear morphological boundaries between the pink and cyan units (Fig. 8a).

### 6.1.3 Multi-color units: HMR, HMR-CaS, IT

Morphologically, HMR, including HMR-CaS, terrains are not distinguishable from the older Mercury IT terrains (IT). Nevertheless, geochemical analysis shows that HMR possess the planet's highest Mg abundance (Vander Kaaden et al., 2017). Table 1 shows that both HMR and HMR-CaS regions are dominated by clinopyroxenes (diopside) and contain <50 wt% plagioclase, > 25 wt% olivine, and >5 wt% sulfides. Whereas, IT is dominated by orthopyroxenes (hypersthene) and contain >50 wt% plagioclase, <2 wt% olivine, and ~4 wt% of

sulfides (Table 1). In the MASCS FCC map (Fig. 7a; Table 1), all three terrains display heterogeneous spectral characteristics, containing all five PC color units, irrespective of their geochemical and mineralogical differences. This suggests that these terrains possess complex geology units, comprised of diverse surface materials with varying silicate mineralogies.

## 7 Discussions and Summary

In this study, we produced a global hyperspectral cube of uniform spatial and spectral resolution from the MASCS observations and applied both standard spectral ratio, slope, and multivariate spectral analysis techniques to understand the compositional and textural diversity of Mercury's regolith. Among the standard spectral analyses, we created visible-slope and visible-slope normalized maps, which highlighted the PD deposits, CB, and the NVP regions. UV-downturn examinations did not differentiate any particular spectral units due to the very coarse spatial resolution of the MASCS datacube. Among the multivariate spectral analysis techniques, the k-means clustering results revealed two major spectral classes closely resembling those observed in the enhanced MDIS color map. On the other hand, the FCC map made from the principal component analysis highlighted variations associated with reflectance, unit age, and regolith texture. Some of the key highlights from this PC color composite analysis includes:

a) Irrespective of the varying geochemical and formation history of the NVP-LMg, CB, PD, and HAI-E geochemical units, their spectral properties derived from PCA are similar (Fig. 7a, 8a).

b) Though RB is predominantly characterized by the green FCC unit, closer inspection finds one pixel of the red (PC1) unit in the basin center and one also sitting on top of the pyroclastic deposits (Suge Facula; 26.09°N 59.68°E) near the southern-eastern rim, in addition to a cyan pixel along the rim (Fig. 7a, 8a). This suggests some geochemical heterogeneity within the RB terrain.

c) NVP-HMg is the only geochemical terrain that is predominantly associated with the pink FCC unit, whereas the HAI-west geochemical unit displays both pink and green FCC units.

d) One of the key findings of the MASCS FCC map is the clear distinction between the NVP-LMg (red FCC unit) and NVP-HMg (pink FCC unit) terrains, which is the first spectrally derived distinction between the two geochemical units. This distinction is not observed in the k-means cluster analysis and associated map.

e) Fig. 8a clearly shows that the pink FCC units mainly represent bright-rayed, fresh craters and fresh hollow materials. Cyan FCC units represent some of the darker LRM observed along the rim of the basins. These correlations suggest that, the PCA results are more representative of the physical properties of the regolith rather than its chemical composition. PCA tends to identify regions associated with freshly exposed materials.

f) Among the geochemical terrains, the IT, HMR and HMR-CaS display mixed, heterogenous characteristics in the MASCS FCC (Fig. 7a, 8a), suggesting both physically and compositionally heterogeneous properties.

## 8 Concluding remarks

Among the multivariate analysis adopted in this study, the principal component analysis (PCA) of MASCS data proves to be an efficient tool which brings out the spectral heterogeneity among the various geochemical terrains of Mercury. One of the major results of this study is the distinction between the low- and high-Mg terrains of the northern volcanic plains seen in the FCC map. However, a direct investigation of the surface mineralogy is still missing. In order to

achieve this, the spectral range beyond the VNIR coverage provided by MESSENGER is required. Here the ESA/JAXA BepiColombo mission can build and extended on MESSNGER. The mid-infrared (MIR; 7-14 μm) spectral region could provide a direct measure of the Si-O abundance of the bulk silicate mineralogy, in addition to identifying the sulfide mineralogy within the hollows. This will be achieved by the MERTIS spectrometer onboard the BepiColombo mission to Mercury. The radiometer channel of MERTIS will investigate the regolith physical properties, such as grain size and thermal inertia, and test the correlation of PC6 with fine-grained, least space-weathered surface materials. VNIR data from the SIMBIO-SYS-VIHI will further add to our understanding of Mercury's VNIR spectral characteristics with its mapping at a higher spatial resolution. In preparation for the BepiColombo measurements at Mercury, future analysis of the MASCS data will focus on detailed spectral mapping of localized surface units, based on the results from this study. In addition, laboratory spectral measurements of fresh and thermally weathered Mercury analogue materials in the VNIR will be used to derive plausible mineral components within the hollows, volcanic materials, and LRM in preparation for the discoveries by BepiColombo. With BepiColombo on its way to Mercury, the global multivariate analysis of the very high spatial resolution hyperspectral VNIR+MIR data from SIMBIO-SYS VIHI and MERTIS will further help to understand the spectral and mineralogical diversities within various geochemical units of Mercury.

## Acknowledgements

I. Varatharajan thanks the DLR/DAAD Doctorate Fellowship for funding her PhD work at PSL-DLR. D. Domingue was supported by NASA's Solar System Workings (SSW) Program, grant 80NSSC18K0521. All MESSENGER data used in this paper are publicly available at the NASA Planetary Data System (PDS).

## References

Besse, S., A. Doressoundiram, and J. Benkhoff (2015), Spectroscopic properties of explosive volcanism within the Caloris basin with MESSENGER observations, Journal of Geophysical Research: Planets, 120(12), 2102-2117, doi:10.1002/2015je004819.

Blewett, D. T., et al. (2011), Hollows on Mercury: MESSENGER Evidence for Geologically Recent Volatile-Related Activity, Science, 333(6051), 1856-1859, doi:10.1126/science.1211681.

Blewett, D. T., C. L. Levy, N. L. Chabot, B. W. Denevi, C. M. Ernst, and S. L. Murchie (2014), Phase-ratio images of the surface of Mercury: Evidence for differences in sub-resolution texture, Icarus, 242, 142-148, doi:https://doi.org/10.1016/j.icarus.2014.08.024.

Blewett, D. T., M. S. Robinson, B. W. Denevi, J. J. Gillis-Davis, J. W. Head, S. C. Solomon, G. M. Holsclaw, and W. E. McClintock (2009), Multispectral images of Mercury from the first MESSENGER flyby: Analysis of global and regional color trends, Earth and Planetary Science Letters, 285(3), 272-282, doi:https://doi.org/10.1016/j.epsl.2009.02.021.

Blewett, D.T., Hawke, B.R., Lucey, P.G., Robinson, M.S., 2007. A Mariner 10 color study of mercurian craters. J. Geophys. Res. 112, E02005. doi:10.1029/2006JE002713.

Blewett, D. T., et al. (2013), Mercury's hollows: Constraints on formation and composition from analysis of geological setting and spectral reflectance, Journal of Geophysical Research: Planets, 118(5), 1013-1032, doi:10.1029/2012je004174.

Bora, M., D. Jyoti, D. Gupta, and A. Kumar (2014), Effect of different distance measures on the performance of K-means algorithm: an experimental study in Matlab, arXiv preprint arXiv:1405.7471.

Bott, N., A. Doressoundiram, F. Zambon, C. Carli, L. Guzzetta, D. Perna, and F. Capaccioni (2019), Global spectral properties and lithology of Mercury: the example of the Shakespeare (H-03) quadrangle, Journal of Geophysical Research: Planets, 0(ja), doi:10.1029/2019je005932.

Byrne, P. K., L. R. Ostrach, C. I. Fassett, C. R. Chapman, B. W. Denevi, A. J. Evans, C. Klimczak, M. E. Banks, J. W. Head, and S. C. Solomon (2016), Widespread effusive volcanism on Mercury likely ended by about 3.5 Ga, Geophysical Research Letters, 43(14), 7408-7416, doi:10.1002/2016gl069412.

D'Incecco, P., J. Helbert, M. D'Amore, A. Maturilli, J. W. Head, R. L. Klima, N. R. Izenberg, W. E. McClintock, H. Hiesinger, and S. Ferrari (2015), Shallow crustal composition of Mercury as revealed by spectral properties and geological units of two impact craters, Planetary and Space Science, 119, 250-263, doi:https://doi.org/10.1016/j.pss.2015.10.007.

De Hon, R., D. Scott, and J. Underwood Jr (1981), Geologic map of the Kuiper (H-6) quadrangle of Mercury, United States Geological Survey, Geologic Investigations Series, Map I-1233.

Denevi, B. W., et al. (2013), The distribution and origin of smooth plains on Mercury, Journal of Geophysical Research: Planets, 118(5), 891-907, doi:10.1002/jgre.20075.

Denevi, B. W., et al. (2009), The Evolution of Mercury's Crust: A Global Perspective from MESSENGER, Science, 324(5927), 613-618, doi:10.1126/science.1172226.

Domingue, D. L., M. D'Amore, S. Ferrari, J. Helbert, and N. R. Izenberg (2019a), Analysis of the MESSENGER MASCS photometric targets part I: Photometric standardization for examining spectral variability across Mercury's surface, Icarus, 319, 247-263, doi:https://doi.org/10.1016/j.icarus.2018.07.019.

Domingue, D. L., M. D'Amore, S. Ferrari, J. Helbert, and N. R. Izenberg (2019b), Analysis of the MESSENGER MASCS photometric targets part II: Photometric variability between geomorphological units, Icarus, 319, 140-246, doi:https://doi.org/10.1016/j.icarus.2018.07.018.

Domingue, D. L., S. L. Murchie, N. L. Chabot, B. W. Denevi, and F. Vilas (2011), Mercury's spectrophotometric properties: Update from the Mercury Dual Imaging System observations during the third MESSENGER flyby, Planetary and Space Science, 59(15), 1853-1872, doi:https://doi.org/10.1016/j.pss.2011.04.012.

Domingue, D. L., S. L. Murchie, B. W. Denevi, C. M. Ernst, and N. L. Chabot (2015), Mercury's global color mosaic: An update from MESSENGER's orbital observations, Icarus, 257, 477-488, doi:https://doi.org/10.1016/j.icarus.2014.11.027.

Goodfellow, I., Y. Bengio, and A. Courville (2016), Deep Learning, MIT Press.

Goudge, T. A., et al. (2014), Global inventory and characterization of pyroclastic deposits on Mercury: New insights into pyroclastic activity from MESSENGER orbital data, Journal of Geophysical Research E: Planets, 119(3), 635-658, doi:10.1002/2013je004480.

Hapke, B., G. E. Danielson Jr., K. Klaasen, and L. Wilson (1975), Photometric observations of Mercury from Mariner 10, Journal of Geophysical Research (1896-1977), 80(17), 2431-2443, doi:10.1029/JB080i017p02431.

Hargitai, H., Á. Kereszturi, and J. Gillis-Davis Pit-Floor Crater, Encyclopedia of Planetary Landforms, 1-6.

Harmon, J. K., M. A. Slade, B. J. Butler, J. W. Head, M. S. Rice, and D. B. Campbell (2007), Mercury: Radar images of the equatorial and midlatitude zones, Icarus, 187(2), 374-405, doi:https://doi.org/10.1016/j.icarus.2006.09.026.

Hawkins, S. E., J. D. Boldt, E. H. Darlington, R. Espiritu, R. E. Gold, B. Gotwols, M. P. Grey, C. D. Hash, J. R. Hayes, and S. E. Jaskulek (2007), The Mercury dual imaging system on the MESSENGER spacecraft, Space Science Reviews, 131(1-4), 247-338.

Helbert, J., A. Maturilli, and M. D'Amore (2013), Visible and near-infrared reflectance spectra of thermally processed synthetic sulfides as a potential analog for the hollow forming materials on Mercury, Earth and Planetary Science Letters, 369–370, 233-238, doi:http://dx.doi.org/10.1016/j.epsl.2013.03.045.

Herrick, R. R., E. M. Bateman, W. G. Crumpacker, and D. Bates (2018), Observations From a Global Database of Impact Craters on Mercury With Diameters Greater than 5 km, Journal of Geophysical Research: Planets, 123(8), 2089-2109, doi:10.1029/2017je005516.

Hiesinger, H., and J. Helbert (2010), The Mercury Radiometer and Thermal Infrared Spectrometer (MERTIS) for the BepiColombo mission, Planetary and Space Science, 58(1–2), 144-165, doi:http://dx.doi.org/10.1016/j.pss.2008.09.019.

Holsclaw, G. M., W. E. McClintock, D. L. Domingue, N. R. Izenberg, D. T. Blewett, and A. L. Sprague (2010), A comparison of the ultraviolet to near-infrared spectral properties of Mercury and the Moon as observed by MESSENGER, Icarus, 209(1), 179-194, doi:https://doi.org/10.1016/j.icarus.2010.05.001.

Hood, L. L. (2016), Magnetic anomalies concentrated near and within Mercury's impact basins: Early mapping and interpretation, Journal of Geophysical Research: Planets, 121(6), 1016-1025, doi:10.1002/2016JE005048.

Izenberg, N. R., et al. (2014), The low-iron, reduced surface of Mercury as seen in spectral reflectance by MESSENGER, Icarus, 228, 364-374, doi:http://dx.doi.org/10.1016/j.icarus.2013.10.023.

Jolliffe, I. (2011), Principal Component Analysis, in International Encyclopedia of Statistical Science, edited by M. Lovric, pp. 1094-1096, Springer Berlin Heidelberg, Berlin, Heidelberg, doi:10.1007/978-3-642-04898-2_455.

Jozwiak, L. M., J. W. Head, and L. Wilson (2018), Explosive volcanism on Mercury: Analysis of vent and deposit morphology and modes of eruption, Icarus, 302, 191-212, doi:https://doi.org/10.1016/j.icarus.2017.11.011.

Kinczyk, M. J., L. M. Prockter, C. R. Chapman, and H. C. M. Susorney. (2016), A Morphological Evaluation of Crater Degradation on Mercury: Revisiting Crater Classification with MESSENGER Data, 47th Lunar and Planetary Science Conference, #1573.

Klima, R. L., B. W. Denevi, C. M. Ernst, S. L. Murchie, and P. N. Peplowski (2018), Global Distribution and Spectral Properties of Low-Reflectance Material on Mercury, Geophysical Research Letters, 45(7), 2945-2953, doi:10.1002/2018gl077544.

Lucey, P. G., and M. A. Riner (2011), The optical effects of small iron particles that darken but do not redden: Evidence of intense space weathering on Mercury, Icarus, 212(2), 451-462, doi:https://doi.org/10.1016/j.icarus.2011.01.022.

MacQueen, J. (1967), Some methods for classification and analysis of multivariate observations, paper presented at Proceedings of the Fifth Berkeley Symposium on Mathematical Statistics and Probability, Volume 1: Statistics, University of California Press, Berkeley, Calif., 1967.

Mancinelli, P., F. Minelli, A. Mondini, C. Pauselli, and C. Federico (2015), A downscaling approach for geological characterization of the Raditladi basin of Mercury, Geological Society, London, Special Publications, 401(1), 57-75, doi:10.1144/sp401.10.

Marchi, S., M. Massironi, G. Cremonese, E. Martellato, L. Giacomini, and L. Prockter (2011), The effects of the target material properties and layering on the crater chronology: The case of Raditladi and Rachmaninoff basins on Mercury, Planetary and Space Science, 59(15), 1968-1980, doi:https://doi.org/10.1016/j.pss.2011.06.007.

Maturilli, A., J. Helbert, I. Varatharajan, and H. Hiesinger (2017), Emissivity Spectra of Analogue Materials at Mercury P-T Conditions, in 48th Lunar and Planetary Science Conference, edited, p. Abstract #1427, Lunar and Planetary Institute, Houston.

McClintock, W. E., and M. R. Lankton (2007), The Mercury Atmospheric and Surface Composition Spectrometer for the MESSENGER Mission, Space Science Reviews, 131(1), 481-521, doi:10.1007/s11214-007-9264-5.

McCord, T. B., and R. N. Clark (1979), The Mercury soil: Presence of Fe2+, Journal of Geophysical Research: Solid Earth, 84(B13), 7664-7668, doi:10.1029/JB084iB13p07664.

Murchie, S. L., R. L. Klima, B. W. Denevi, C. M. Ernst, M. R. Keller, D. L. Domingue, D. T. Blewett, N. L. Chabot, C. D. Hash, and E. Malaret (2015), Orbital multispectral mapping of Mercury with the MESSENGER Mercury Dual Imaging System: Evidence for the origins of plains units and low-reflectance material, Icarus, 254, 287-305.

Murchie, S. L., T. R. Watters, M. S. Robinson, J. W. Head, R. G. Strom, C. R. Chapman, S. C. Solomon, W. E. McClintock, L. M. Prockter, and D. L. Domingue (2008), Geology of the Caloris basin, Mercury: A view from MESSENGER, Science, 321(5885), 73-76.

Namur, O., and B. Charlier (2017), Silicate mineralogy at the surface of Mercury, Nature Geosci, 10(1), 9-13, doi:10.1038/ngeo2860

Neukum, G., J. Oberst, H. Hoffmann, R. Wagner, and B. A. Ivanov (2001), Geologic evolution and cratering history of Mercury, Planetary and Space Science, 49(14), 1507-1521, doi:https://doi.org/10.1016/S0032-0633(01)00089-7.

Peplowski, P. N., R. L. Klima, D. J. Lawrence, C. M. Ernst, B. W. Denevi, E. A. Frank, J. O. Goldsten, S. L. Murchie, L. R. Nittler, and S. C. Solomon (2016), Remote sensing evidence for an ancient carbon-bearing crust on Mercury, Nature Geoscience, 9, 273, doi:10.1038/ngeo2669

Peplowski, P. N., D. J. Lawrence, W. C. Feldman, J. O. Goldsten, D. Bazell, L. G. Evans, J. W. Head, L. R. Nittler, S. C. Solomon, and S. Z. Weider (2015), Geochemical terrains of Mercury's northern hemisphere as revealed by MESSENGER neutron measurements, Icarus, 253, 346-363.
Robinson, M. S., et al. (2008), Reflectance and Color Variations on Mercury: Regolith Processes and Compositional Heterogeneity, Science, 321(5885), 66-69, doi:10.1126/science.1160080.

Robinson, M.S., Lucey, P.G.,1997. Recalibrated Mariner 10 color mosaics: implications for mercurian volcanism. Science 275, 197–200.

Solomon, S. C., et al. (2001), The MESSENGER mission to Mercury: scientific objectives and implementation, Planetary and Space Science, 49(14), 1445-1465, doi:https://doi.org/10.1016/S0032-0633(01)00085-X.

Spudis, P. D., and J. E. Guest (1988), Stratigraphy and geologic history of Mercury, Mercury, 118-164.

Thomas, R. J., D. A. Rothery, S. J. Conway, and M. Anand (2014), Hollows on Mercury: Materials and mechanisms involved in their formation, Icarus, 229, 221-235.

Trang, D., P. G. Lucey, and N. R. Izenberg (2017), Radiative transfer modeling of MESSENGER VIRS spectra: Detection and mapping of submicroscopic iron and carbon, Icarus, 293, 206-217, doi:https://doi.org/10.1016/j.icarus.2017.04.026.

Vander Kaaden, K. E., F. M. McCubbin, L. R. Nittler, P. N. Peplowski, S. Z. Weider, E. A. Frank, and T. J. McCoy (2017), Geochemistry, mineralogy, and petrology of boninitic and komatiitic rocks on the mercurian surface: Insights into the mercurian mantle, Icarus, 285, 155-168, doi:http://dx.doi.org/10.1016/j.icarus.2016.11.041.

Varatharajan, I., A. Maturilli, J. Helbert, G. Alemanno, and H. Hiesinger (2019), Spectral behavior of sulfides in simulated daytime surface conditions of Mercury: Supporting past (MESSENGER) and future missions (BepiColombo), Earth and Planetary Science Letters, 520, 127-140, doi:https://doi.org/10.1016/j.epsl.2019.05.020.

Vilas, F., et al. (2016), Mineralogical indicators of Mercury's hollows composition in MESSENGER color observations, Geophysical Research Letters, 43(4), 1450-1456, doi:10.1002/2015gl067515.

Vilas, F., M. A. Leake, and W. W. Mendell (1984), The dependence of reflectance spectra of Mercury on surface terrain, Icarus, 59(1), 60-68, doi:https://doi.org/10.1016/0019-1035(84)90055-1.

Vilas, F., and T. B. McCord (1976), Mercury: Spectral reflectance measurements (0.33–1.06 μm) 1974/1975, Icarus, 28(4), 593-599, doi:https://doi.org/10.1016/0019-1035(76)90132-9.

Watters, T. R., J. W. Head, S. C. Solomon, M. S. Robinson, C. R. Chapman, B. W. Denevi, C. I. Fassett, S. L. Murchie, and R. G. Strom (2009), Evolution of the Rembrandt Impact Basin on Mercury, Science, 324(5927), 618-621, doi:10.1126/science.1172109.

Weider, S. Z., et al. (2015), Evidence for geochemical terrains on Mercury: Global mapping of major elements with MESSENGER's X-Ray Spectrometer, Earth and Planetary Science Letters, 416, 109-120, doi:https://doi.org/10.1016/j.epsl.2015.01.023.

Whitten, J. L., and J. W. Head (2015), Rembrandt impact basin: Distinguishing between volcanic and impact-produced plains on Mercury, Icarus, 258, 350-365, doi:https://doi.org/10.1016/j.icarus.2015.06.022.

Xiao, Z., R. G. Strom, D. T. Blewett, P. K. Byrne, S. C. Solomon, S. L. Murchie, A. L. Sprague, D. L. Domingue, and J. Helbert (2013), Dark spots on Mercury: A distinctive low-reflectance material and its relation to hollows, Journal of Geophysical Research: Planets, 118(9), 1752-1765, doi:10.1002/jgre.20115.